Quantum Crystal Structure in the 250 K Superconducting Lanthanum Hydride

Ion Errea,[1,2,3] Francesco Belli,[1,2] Lorenzo Monacelli,[4] Antonio Sanna,[5] Takashi Koretsune,[6] Terumasa Tadano,[7] Raffaello Bianco,[2] Matteo Calandra,[8] Ryotaro Arita,[9,10] Francesco Mauri,[4,11] and José A. Flores-Livas[4]

[1] *Fisika Aplikatua 1 Saila, Gipuzkoako Ingeniaritza Eskola, University of the Basque Country (UPV/EHU), Europa Plaza 1, 20018 Donostia/San Sebastián, Spain*
[2] *Centro de Física de Materiales (CSIC-UPV/EHU), Manuel de Lardizabal Pasealekua 5, 20018 Donostia/San Sebastián, Spain*
[3] *Donostia International Physics Center (DIPC), Manuel de Lardizabal Pasealekua 4, 20018 Donostia/San Sebastián, Spain*
[4] *Dipartimento di Fisica, Università di Roma La Sapienza, Piazzale Aldo Moro 5, I-00185 Roma, Italy*
[5] *Max-Planck Institute of Microstructure Physics, Weinberg 2, 06120 Halle, Germany*
[6] *Department of Physics, Tohoku University, 6-3 Aza-Aoba, Sendai, 980-8578 Japan*
[7] *Research Center for Magnetic and Spintronic Materials, National Institute for Materials Science, Tsukuba 305-0047, Japan*
[8] *Sorbonne Université, CNRS, Institut des Nanosciences de Paris, UMR7588, F-75252, Paris, France*
[9] *Department of Applied Physics, University of Tokyo, 7-3-1 Hongo Bunkyo-ku, Tokyo 113-8656 Japan*
[10] *RIKEN Center for Emergent Matter Science, 2-1 Hirosawa, Wako, 351-0198, Japan*
[11] *Graphene Labs, Fondazione Istituto Italiano di Tecnologia, Via Morego, I-16163 Genova, Italy*

(Dated: July 30, 2019)

The discovery of superconductivity at 200 K in the hydrogen sulfide system at large pressures [1] was a clear demonstration that hydrogen-rich materials can be high-temperature superconductors. The recent synthesis of LaH_{10} with a superconducting critical temperature (T_c) of 250 K [2, 3] places these materials at the verge of reaching the long-dreamed room-temperature superconductivity. Electrical and x-ray diffraction measurements determined a weakly pressure-dependent T_c for LaH_{10} between 137 and 218 gigapascals in a structure with a face-centered cubic (fcc) arrangement of La atoms [3]. Here we show that quantum atomic fluctuations stabilize in all this pressure range a high-symmetry Fm-3m crystal structure consistent with experiments, which has a colossal electron-phonon coupling of $\lambda \sim 3.5$. Even if *ab initio* classical calculations neglecting quantum atomic vibrations predict this structure to distort below 230 GPa yielding a complex energy landscape with many local minima, the inclusion of quantum effects simplifies the energy landscape evidencing the Fm-3m as the true ground state. The agreement between the calculated and experimental T_c values further supports this phase as responsible for the 250 K superconductivity. The relevance of quantum fluctuations in the energy landscape found here questions many of the crystal structure predictions made for hydrides within a classical approach that at the moment guide the experimental quest for room-temperature superconductivity [4–6]. Furthermore, quantum effects reveal crucial to sustain solids with extraordinary electron-phonon coupling that may otherwise be unstable [7].

The potential of metallic hydrogen as a high-T_c superconductor [8, 9] was identified few years after the development of the Bardeen-Cooper-Schrieffer (BCS) theory, which explained superconductivity through the electron-phonon coupling mechanism. The main argument was that T_c can be maximized for light compounds due to their high vibrational frequencies. In view of the large pressures needed to metallize hydrogen [10], chemical pre-compression with heavier atoms [11, 12] was suggested as a pathway to decrease the pressure needed to reach metallicity and, thus, superconductivity. These ideas have bloomed thanks to modern *ab initio* crystal structure prediction methods based on density-functional theory (DFT) [5, 13, 14]. Hundreds of hydrogen-rich compounds have been predicted to be thermodynamically stable at high pressures and, by calculating the electron-phonon interaction parameters, their T_c's have been estimated [4, 5]. The success of this symbiosis between DFT crystal structure predictions and T_c calculations is exemplified by the discovery of superconductivity in H_3S at 200 K [1, 15, 16]. The prospects for discovering warm hydrogen-based superconductors in the next years are thus high, in clear contrast with other high-T_c superconducting families such as cuprates or pnictides [17, 18], where the lack of a clear understanding of the superconducting mechanism hinders an *in silico* guided approach.

DFT predictions in the La-H system proposed LaH_{10} to be thermodynamically stable against decomposition above 150 GPa. A sodalite type-structure with space group Fm-3m and T_c∼280 K was suggested above ∼220 GPa (see Fig. 1), and a distorted version of it below with space group $C2/m$ and a rhombohedral La sublattice [19, 20]. By laser heating a lanthanum sample in a hydrogen-rich atmosphere within a diamond anvil cell (DAC), a lanthanum superhydride was synthesized right after [20]. Based on the unit cell volume obtained by x-ray diffraction, the hydrogen to lanthanum ratio was estimated to be between 9 and 12. An fcc arrangement of the La atoms was determined above ∼160 GPa, and a rhombohedral lattice below with R-3m space group for the La sublattice. Due to the small x-ray cross section of hydrogen, experimentally it is not possible to resolve directly the H sublattice. Early this year, evidences of a superconducting transition at 260 K and 188 GPa were reported in a lanthanum superhydride [2]. These findings were confirmed and put in solid grounds few months later

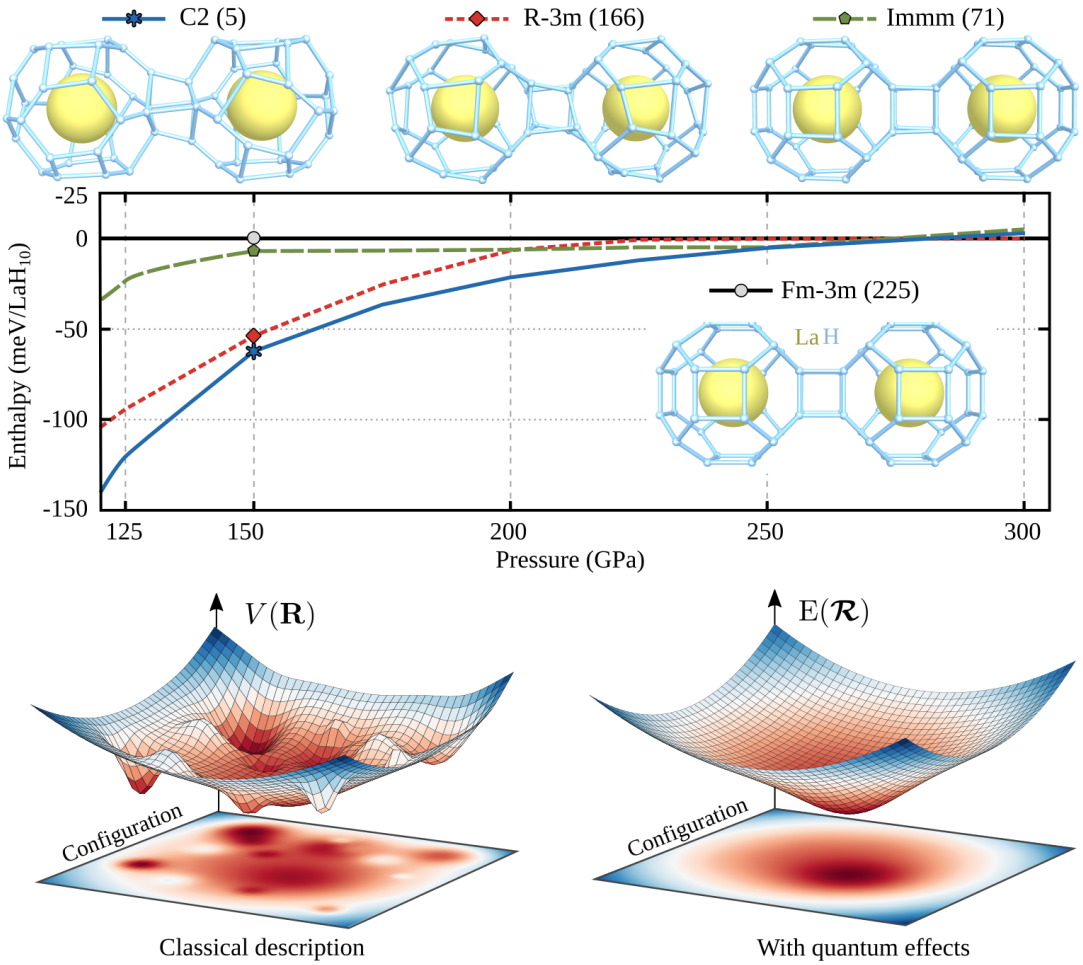

Figure 1. **Quantum effects stabilize the symmetric Fm-3m phase of LaH_{10}.** Top panel: Enthalpy as function of pressure for different structures of LaH_{10} calculated neglecting the zero-point energy. The pressure in the figure is calculated from $V(\mathbf{R})$, neglecting quantum effects on it. The crystal structure of the different phases found are shown. Bottom left: Sketch of a Born-Oppenheimer energy surface $V(\mathbf{R})$ exemplifying the presence of many local minima for many distorted structures. $\mathbf{R}$ represents the positions of atoms treated classically as simple points. Bottom right: sketch of the configurational $E(\boldsymbol{\mathcal{R}})$ energy surface including quantum effects. $\boldsymbol{\mathcal{R}}$ represents the quantum centroid positions, which determine the center of the ionic wave functions, i.e., the average atomic positions. All phases collapse to a single phase, the highly symmetric Fm-3m.

by an independent group that measured a T_c of 250 K from 137 to 218 GPa in a structure with fcc arrangement of the La atoms and suggested a LaH_{10} stoichiometry [3].

Even if it is tempting to assign the record superconductivity to the Fm-3m phase predicted previously [2, 3], there is a clear problem: the Fm-3m structure is predicted to be dynamically unstable in the whole pressure range where a 250 K T_c was observed. This implies that this phase is not a minimum of the Born-Oppenheimer energy surface. Consequently, no T_c has been estimated for this phase in the experimental pressure range. Considering that quantum proton fluctuations symmetrize hydrogen bonds in the high-pressure X phase of ice [21] and in H_3S [22, 23], this contradiction may signal a problem of the classical treatment of the atomic vibrations in the calculations. We show here how quantum atomic fluctuations completely reshape the energy landscape making the Fm-3m phase the true ground state and the responsible for the observed superconducting critical temperature.

We start by calculating with DFT the lowest enthalpy structures of LaH_{10} as a function of pressure with state-of-the-art crystal structure prediction methods [24, 25]. The contribution associated with atomic fluctuations is not included, so that the energy just corresponds to the Born-Oppenheimer energy $V(\mathbf{R})$, where $\mathbf{R}$ represents the position of atoms treated classically as simple points. As shown in Figure 1, different distorted phases of LaH_{10} are thermodynamically more stable than the Fm-3m phase. Above ∼250 GPa all phases merge to the Fm-3m symmetric phase. These results are in agreement with previous calculations [19], even if we identify other possible distorted structures with lower enthalpy such as

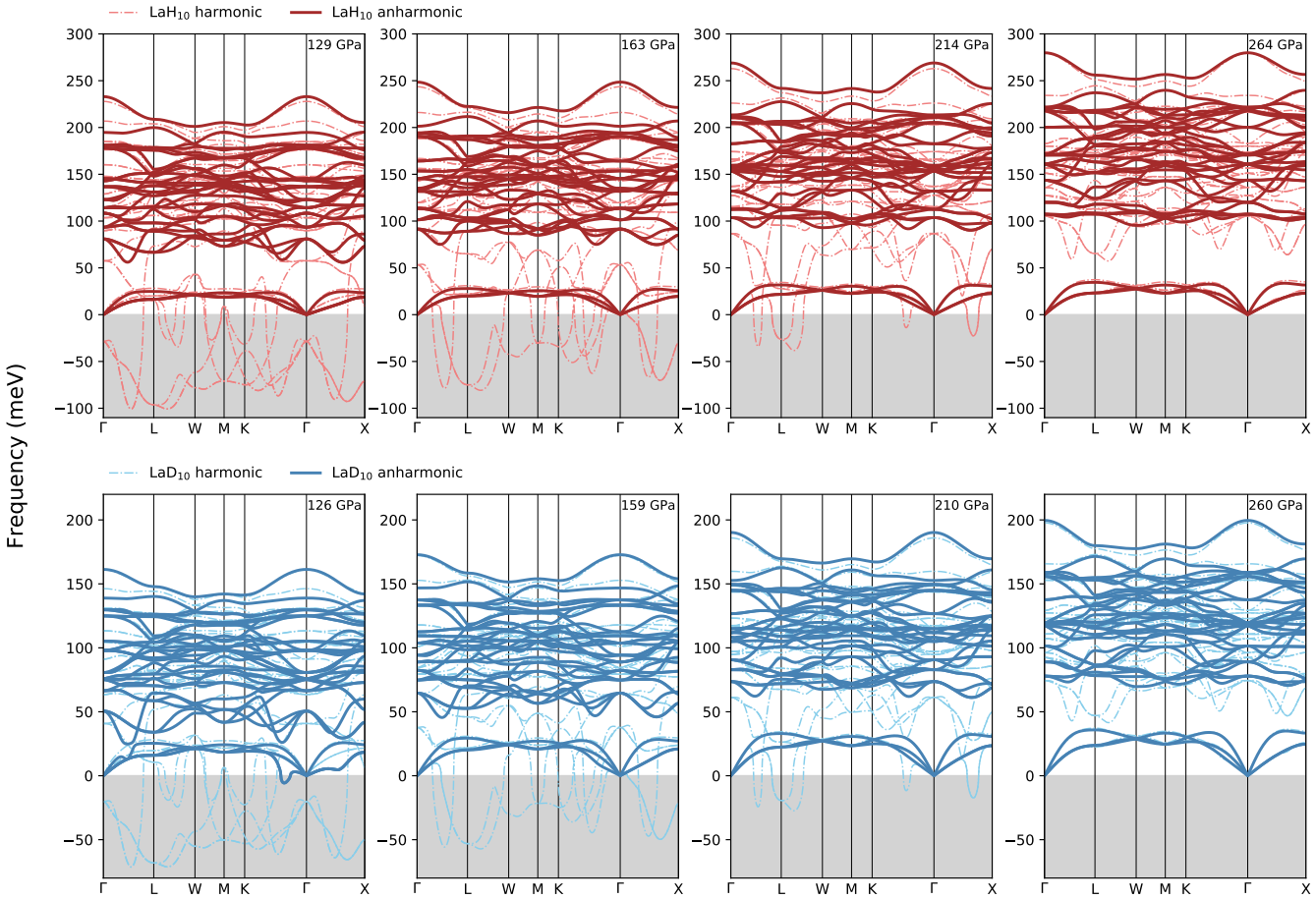

Figure 2. **Phonon band structure of Fm-3m LaH_{10} at different pressures.** The harmonic phonons show large instabilities in several regions of the Brillouin zone. Only at the high-pressure limit, e.g. above 220-250 GPa dynamic (harmonic) stabilization is reached. The anharmonic phonons obtained from the Hessian of the quantum $E(\boldsymbol{\mathcal{R}})$ energy within the SSCHA are dynamically stable in the experimentally relevant range. The case of deuterium develops a instability at low pressures (126 GPa) consistent with experimental evidence. The pressure given corresponds to the calculated from $E(\boldsymbol{\mathcal{R}})$ that considers quantum effects. The grey area marks the region with imaginary phonon frequencies, which are depicted as negative frequencies.

the R-3m, $C2$ and $P1$ (not shown) phases. These phases not only imply a distortion of the H atoms, also show a La sublattice without an fcc arrangement, and thus should be detectable by x-ray. The fact that many structures are predicted underlines that the classical $V(\mathbf{R})$ energy surface is of a multifunnel structure tractable to many different saddle and local minima, as sketched in Figure 1.

This picture completely changes when including the energy of quantum atomic fluctuations, the zero-point energy (ZPE). We calculate the ZPE within the stochastic self-consistent harmonic approximation (SSCHA) [26–28]. The SSCHA is a variational method that calculates the $E(\boldsymbol{\mathcal{R}})$ energy of the system including atomic quantum fluctuations as a function of the *centroid* positions $\boldsymbol{\mathcal{R}}$, which determine the center of the ionic wave functions. The calculations are performed without approximating the $V(\mathbf{R})$ potential, keeping all its anharmonic terms. We perform a minimization of $E(\boldsymbol{\mathcal{R}})$ and determine the centroid positions at its minimum. By calculating the stress tensor from $E(\boldsymbol{\mathcal{R}})$ [28], we relax the lattice parameters seeking for structures with isotropic stress conditions considering quantum effects. We start the quantum relaxation for both R-3m and $C2$ phases with the lattice that yields a classical isotropic pressure of 150 GPa and vanishing classical forces, i.e., calculated from $V(\mathbf{R})$. All quantum relaxations quickly evolve into the Fm-3m phase. This suggests that the quantum $E(\boldsymbol{\mathcal{R}})$ energy landscape is much simpler than the classical $V(\mathbf{R})$ as sketched in Figure 1. And that the sodalite symmetric Fm-3m phase is the ground state for LaH_{10} in all the pressure range of interest. Quantum effects are colossal: reshaping the energy landscape and stabilizing structures by more than 60 meV per LaH_{10}.

Our results further confirm that the structure of LaH_{10} responsible for the 250 K superconductivity is Fm-3m. This is completely consistent with the fcc arrangement of La atoms found experimentally [3]. However, Geballe et al. [20] observed a rhombohedral distortion below ∼160

GPa, with an R-3m space group for the La sublattice and a rhombohedral angle of approximately 61.3°($c/a \sim 2.38$ in the hexagonal representation). Our calculations show that this distortion is compatible with slight anisotropic stress conditions in the DAC. Indeed, performing a SSCHA minimization for our R-3m phase but keeping the rhombohedral angle fixed at 62.3°(the value that yields an isotropic pressure of 150 GPa at the classical level) the quantum stress tensor shows a 6% anisotropy between the diagonal direction and the perpendicular plane. This suggests that anisotropic conditions inside the DAC can produce the R-3m phase, while other experimental stress conditions could favor other crystal phases.

The Fm-3m phonon spectra calculated in the harmonic approximation from the Hessian of $V(\mathbf{R})$ show clear phonon instabilities in a broad region of the Brillouin zone (see Figure 2). These instabilities appear below ∼230 GPa. This is consistent with the fact that below this pressure many possible atomic distortions lower the enthalpy of this phase. On the contrary, as shown in Figure 2, when calculating the phonons from the Hessian of $E(\boldsymbol{\mathcal{R}})$ [27], which effectively captures the full anharmonicity of $V(\mathbf{R})$, no instability is observed. This confirms again that the Fm-3m phase is a minimum in the quantum-energy landscape in the whole pressure range where a 250 K T_c was observed. While the Fm-3m phase of LaH_{10} remains a minimum of $E(\boldsymbol{\mathcal{R}})$ as low as ∼ 129 GPa, the case of LaD_{10} shows instabilities at 126 GPa, implying that at this pressure the Fm-3m phase of LaD_{10} distorts to a new phase (as suggested by Drozdov et al. [3]). Below this pressure we also predict that LaH_{10} composition is not longer thermodynamically stable and low-hydrogen compositions are likely to occur.

Flagrantly, the breakdown of the classical harmonic approximation for phonons makes impossible the estimation of T_c below ∼250 GPa in the Fm-3m phase and questions all previous calculations [19, 29]. Indeed, the anharmonic phonon renormalization remains huge also at 264 GPa (see Figure 2). On the contrary, with anharmonic phonons derived from the Hessian of $E(\boldsymbol{\mathcal{R}})$ we can readily calculate the electron-phonon interaction and the superconducting T_c in the experimental range of pressure (120–210 GPa). The superconducting critical temperature is estimated fully *ab initio* –without any empirical parameter– by solving Migdal-Éliashberg (ME) equations and applying SuperConducting DFT (SCDFT). As shown in Figure 3, the numerical solutions of ME equations with anisotropic energy gap are almost on top of the experimental values. SCDFT values systematically show a slightly lower T_c. Our reported values of T_c evidence the phonon-driven mechanism of superconductivity and confirm LaH_{10} in its Fm-3m structure as responsible for the highest-T_c up to date reported. Our calculations for LaD_{10} in the Fm-3m phase are also in agreement with the experimental point reported. Despite the large anharmonic effects at play, the isotope coefficient

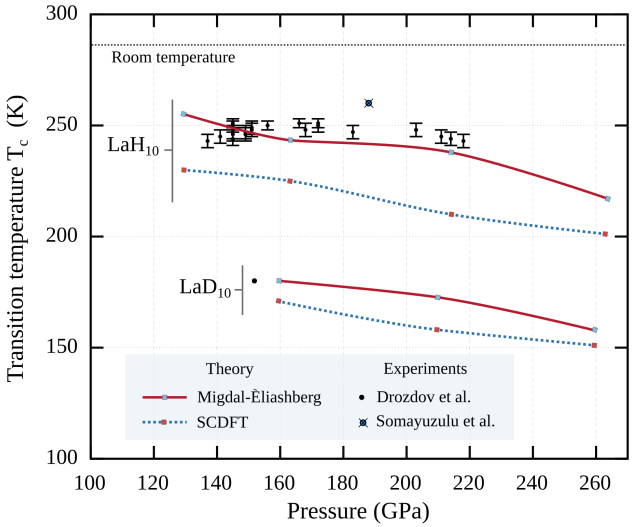

Figure 3. **Summary of experimental and theoretical T_c values.** Superconducting critical temperatures calculated within anisotropic Migdal-Éliashberg equations and SCDFT. In both cases the anharmonic phonons obtained with the SSCHA are used. The results are compared with the experimental measurements by Somayuzulu et al. [2] and Drozdov et al. [3].

$\alpha = -\left[\ln T_c(LaD_{10}) - \ln T_c(LaH_{10})\right] / \ln 2$ is close to 0.5 (0.43 around 160 GPa), the expected value in BCS theory, and it is in agreement with the experimentally reported $\alpha = 0.46$.

We finally check T_c for the subtle rhombohedral distortion that could be induced by anisotropic stress conditions of pressure. Fixing the rhombohedral angle at 62.3° the obtained T_c for the R-3m phase at 160 GPa is a 9% lower than for the Fm-3m. Thus, the observed weak pressure dependence of T_c is consistent with the absence of a rhombohedral distortion, as suggested by the x-ray data [3]. However, as argued above, undesired anisotropic stress conditions in the DAC can induce phase transitions. We thus believe that other experimental T_c measurements with lower values but around 200 K correspond to distorted structures induced by anisotropic conditions of pressure. In fact, we can safely rule out that compositions such as LaH_{11}, proposed to yield a high critical temperature [3], is responsible for any sizable T_c (see Extended Data).

In summary, this work demonstrates how quantum effects are of capital importance in determining the ground state structures of superconducting hydrides, challenging all current predictions and evidencing flaws in standard theoretical methods. It also illustrates that quantum fluctuations are indispensable to sustain crystals with huge λ's (λ reaches a record value of 3.6 at 129 GPa for LaH_{10}) that be otherwise destabilized by the colossal electron-phonon interaction to distorted (low symmetry)

structures reducing the electronic density of states at the Fermi level (see Extended Data) [7]. This is relevant since large λ is required to guarantee high-T_c [5, 6], not simply light atomic masses.

[1] A. P. Drozdov, M. I. Eremets, I. A. Troyan, V. Ksenofontov, and S. I. Shylin. Conventional superconductivity at 203 kelvin at high pressures in the sulfur hydride system. *Nature*, 525:73, 2015.

[2] Maddury Somayazulu, Muhtar Ahart, Ajay K. Mishra, Zachary M. Geballe, Maria Baldini, Yue Meng, Viktor V. Struzhkin, and Russell J. Hemley. Evidence for superconductivity above 260 K in lanthanum superhydride at megabar pressures. *Phys. Rev. Lett.*, 122:027001, 2019.

[3] A. P. Drozdov, P. P. Kong, V. S. Minkov, S. P. Besedin, M. A. Kuzovnikov, S. Mozaffari, L. Balicas, F. F. Balakirev, D. E. Graf, V. B. Prakapenka, E. Greenberg, D. A. Knyazev, M. Tkacz, and M. I. Eremets. Superconductivity at 250 K in lanthanum hydride under high pressures. *Nature*, 569:528, 2019.

[4] Tiange Bi, Niloofar Zarifi, Tyson Terpstra, and Eva Zurek. The search for superconductivity in high pressure hydrides. *arXiv preprint arXiv:1806.00163*, 2018.

[5] José A. Flores-Livas, Lilia Boeri, Antonio Sanna, Gianni Profeta, Ryotaro Arita, and Mikhail Eremets. A Perspective on Conventional High-Temperature Superconductors at High Pressure: Methods and Materials. *arXiv e-prints*, page arXiv:1905.06693, 2019.

[6] Chris J. Pickard, Ion Errea, and Mikhail I. Eremets. *to be published in Annual Review of Condensed Matter Physics*, 2019.

[7] Philip B. Allen and Marvin L. Cohen. Superconductivity and Phonon Softening. *Phys. Rev. Lett.*, 29:1593, 1972.

[8] N. Ashcroft. Metallic hydrogen: A high-temperature superconductor? *Phys. Rev. Lett.*, 21:1748, 1968.

[9] Vitalii L. Ginzburg. Superfluidity and superconductivity in the universe. *Journal of Statistical Physics*, 1:3, 1969.

[10] Ranga P. Dias and Isaac F. Silvera. Observation of the wigner-huntington transition to metallic hydrogen. *Science*, 355:715, 2017.

[11] J. J. Gilman. Lithium dihydrogen fluoride—an approach to metallic hydrogen. *Phys. Rev. Lett.*, 26:546, 1971.

[12] N. W. Ashcroft. Hydrogen dominant metallic alloys: High temperature superconductors? *Phys. Rev. Lett.*, 92:187002, 2004.

[13] Lijun Zhang, Yanchao Wang, Jian Lv, and Yanming Ma. Materials discovery at high pressures. *Nature Reviews Materials*, 2:17005, 2017.

[14] Artem R. Oganov, Chris J. Pickard, Qiang Zhu, and Richard J. Needs. Structure prediction drives materials discovery. *Nature Reviews Materials*, 4:331, 2019.

[15] Yinwei Li, Jian Hao, Hanyu Liu, Yanling Li, and Yanming Ma. The metallization and superconductivity of dense hydrogen sulfide. *The Journal of Chemical Physics*, 140:174712, 2014.

[16] Defang Duan, Yunxian Liu, Fubo Tian, Da Li, Xiaoli Huang, Zhonglong Zhao, Hongyu Yu, Bingbing Liu, Wenjing Tian, and Tian Cui. Pressure-induced metallization of dense $(H_2S)_2H_2$ with high-Tc superconductivity. *Sci. Rep.*, 4:6968, 2014.

[17] A. Schilling, M. Cantoni, J. D. Guo, and H. R. Ott. Superconductivity above 130 K in the Hg–Ba–Ca–Cu–O system. *Nature*, 363:56, 1993.

[18] Yoichi Kamihara, Hidenori Hiramatsu, Masahiro Hirano, Ryuto Kawamura, Hiroshi Yanagi, Toshio Kamiya, and Hideo Hosono. Iron-based layered superconductor: LaOFeP. *Journal of the American Chemical Society*, 128:10012, 2006.

[19] Hanyu Liu, Ivan I. Naumov, Roald Hoffmann, N.W. Ashcroft, and Russell J. Hemley. Potential high-Tc superconducting lanthanum and yttrium hydrides at high pressure. *Proceedings of the National Academy of Sciences*, 114:6990, 2017.

[20] Zachary M. Geballe, Hanyu Liu, Ajay K. Mishra, Muhtar Ahart, Maddury Somayazulu, Yue Meng, Maria Baldini, and Russell J. Hemley. Synthesis and stability of lanthanum superhydrides. *Angewandte Chemie International Edition*, 57:688, 2018.

[21] Magali Benoit, Dominik Marx, and Michele Parrinello. Tunnelling and zero-point motion in high-pressure ice. *Nature*, 392:258, 1998.

[22] Ion Errea, Matteo Calandra, Chris J. Pickard, Joseph R. Nelson, Richard J. Needs, Yinwei Li, Hanyu Liu, Yunwei Zhang, Yanming Ma, and Francesco Mauri. Quantum hydrogen-bond symmetrization in the superconducting hydrogen sulfide system. *Nature*, 532:81, 2016.

[23] Raffaello Bianco, Ion Errea, Matteo Calandra, and Francesco Mauri. High-pressure phase diagram of hydrogen and deuterium sulfides from first principles: Structural and vibrational properties including quantum and anharmonic effects. *Phys. Rev. B*, 97:214101, 2018.

[24] Stefan Goedecker. Minima hopping: An efficient search method for the global minimum of the potential energy surface of complex molecular systems. *The Journal of Chemical Physics*, 120:9911, 2004.

[25] M. Amsler and S. Goedecker. Crystal structure prediction using the minima hopping method. *The Journal of Chemical Physics*, 133:224104, 2010.

[26] Ion Errea, Matteo Calandra, and Francesco Mauri. Anharmonic free energies and phonon dispersions from the stochastic self-consistent harmonic approximation: Application to platinum and palladium hydrides. *Phys. Rev. B*, 89:064302, 2014.

[27] Raffaello Bianco, Ion Errea, Lorenzo Paulatto, Matteo Calandra, and Francesco Mauri. Second-order structural phase transitions, free energy curvature, and temperature-dependent anharmonic phonons in the self-consistent harmonic approximation: Theory and stochastic implementation. *Phys. Rev. B*, 96:014111, 2017.

[28] Lorenzo Monacelli, Ion Errea, Matteo Calandra, and Francesco Mauri. Pressure and stress tensor of complex anharmonic crystals within the stochastic self-consistent harmonic approximation. *Phys. Rev. B*, 98:024106, 2018.

[29] Liangliang Liu, Chongze Wang, Seho Yi, Kun Woo Kim, Jaeyong Kim, and Jun-Hyung Cho. Microscopic mechanism of room-temperature superconductivity in compressed LaH_{10}. *Phys. Rev. B*, 99:140501, 2019.

Acknowledgements. This research was supported by the European Research Council (ERC) under the European Unions Horizon 2020 research and innovation programme (grant agreement No. 802533); the Spanish Ministry of Economy and Competitiveness (FIS2016-76617-P); NCCR MARVEL funded by the Swiss National

Science Foundation; and grant-in-Aid for Scientific Research (No.16H06345, 18K03442 and No. 19H05825) from the Ministry of Education, Culture, Sports, Science and Technology, Japan. Computational resources were provided by the Barcelona Superconducting Center (project FI-2019-1-0031) and the Swiss National Supercomputing Center (CSCS).

Author contributions. The project was conceived by I.E. and J.A.F.-L. The SSCHA was developed by I.E., L.M., R.B., M.C. and F.M. In particular, R.B. developed the method to compute the quantum energy Hessian and the anharmonic phonon dispersions, and L.M. developed the method to perform a quantum relaxation of the lattice parameters. I.E. and F.B. performed the SSCHA calculations. A.S. T.K., T.T., R.A. and J.A.F.-L. conducted studies on structure prediction and superconductivity. All authors contributed to the editing of the manuscript.

Competing interests. The authors declare no competing interests.

Methods

Calculation details. First-principles calculations were performed within DFT and the generalized gradient approximation (GGA) as parametrized by Perdew, Burke, and Ernzerhof (PBE) [30]. Harmonic phonon frequencies were calculated within density functional perturbation theory (DFPT) [31] making use of the Quantum ESPRESSO code [32, 33]. The SSCHA [26–28, 34] minimization requires the calculation of energies, forces and stress tensors in supercells. These were calculated as well within DFT at the PBE level with Quantum ESPRESSO. For the final SSCHA populations, 1000 configurations were used to reduce the stochastic noise. In all these calculations we used ultrasoft pseudopotentials including 11 electrons for the La atoms, a plane-wave cut-off energy of 50 Ry for the kinetic energy and 500 Ry for the charge density.

In the harmonic phonon calculations for the Fm-$3m$ and R-$3m$ phases, we used the primitive and rhombohedral lattices, respectively, with one LaH_{10} formula unit in the unit cell. A 20×20×20 Monkhorst-Pack shifted electron-momentum grid was used for these calculations with a Methfessel-Paxton smearing of 0.02 Ry. The DFT calculations performed for the SSCHA on supercells were performed on a coarser electron-momentum grid, which would correspond to a 12×12×12 grid in the unit cell. We explicitly verified that this coarser mesh yields a fully converged SSCHA gradient with respect to the electron-momentum grid, thus, not affecting the SSCHA minimization. The DFT supercell calculations for the SSCHA minimization on the $C2$ phase were performed keeping the same **k**-point density.

All phonon frequencies for **q**-points not commensurate with the supercell used in the SSCHA minimization were obtained by directly Fourier interpolating the real space force constants obtained in this supercell, which are calculated form the Hessian of $E(\boldsymbol{\mathcal{R}})$. For the Fm-$3m$ phase the SSCHA calculation was performed both on a 2×2×2 and 3×3×3 supercell containing, respectively, 88 and 297 atoms. The phonon spectra shown in Figure 2 for the Fm-$3m$ phase are obtained by Fourier interpolating directly the SSCHA energy Hessian force constants obtained in a 3×3×3 supercell. In Extended Data Figure 2 we show that the phonon spectrum obtained interpolating directly the force constants in a 2×2×2 supercell yields similar results, indicating that the energy Hessian force constants are short-range and can be Fourier interpolated. Indeed, the T_c calculated with the 2×2×2 and 3×3×3 force constants for interpolating phonons only differs in approximately 3 K. Upon this, the SSCHA quantum structural relaxations in the R-$3m$ and $C2$ phases were performed in supercells with 88 atoms.

As shown in Ref. [27], the Hessian of $E(\boldsymbol{\mathcal{R}})$ is

$$\frac{\partial^2 E(\boldsymbol{\mathcal{R}})}{\partial \boldsymbol{\mathcal{R}} \partial \boldsymbol{\mathcal{R}}} = \boldsymbol{\Phi} + \overset{(3)}{\boldsymbol{\Phi}} \boldsymbol{\Lambda} \left[\mathbf{1} - \overset{(4)}{\boldsymbol{\Phi}} \boldsymbol{\Lambda} \right]^{-1} \overset{(3)}{\boldsymbol{\Phi}}. \tag{1}$$

Bold notation represents matrices and tensors in compact notation. In Eq. (1), $\boldsymbol{\Phi}$ are the variational force constants of the SSCHA minimization, $\overset{(n)}{\boldsymbol{\Phi}}$ the quantum statistical averages taken with the SSCHA density matrix of the n-th order derivatives of $V(\mathbf{R})$, and $\boldsymbol{\Lambda}$ a tensor that depends on the temperature and $\boldsymbol{\Phi}$. $\mathbf{1}$ is the identity matrix. As we show in Extended Figure 3, setting $\overset{(4)}{\boldsymbol{\Phi}} = 0$ has a negligible effect on the phonons obtained from the Hessian defined in Eq. (1). Therefore, $\overset{(4)}{\boldsymbol{\Phi}}$ is neglected throughout, and all superconductivity calculations in the Fm-$3m$ and R-$3m$ phases are performed making use of the phonon frequencies and polarization vectors obtained from the Hessian of $E(\boldsymbol{\mathcal{R}})$ with $\overset{(4)}{\boldsymbol{\Phi}} = 0$. We also estimated T_c with the phonon frequencies and polarization vectors obtained instead from $\boldsymbol{\Phi}$, resulting in a critical temperature 12 K lower within Allen-Dynes modified McMillan equation. This difference is small and within the uncertainty of the T_c calculation between SCDFT and anisotropic Migdal-Éliashberg calculations (see Figure 3 and below).

The Éliashberg spectral function, which we used for the T_c calculations, is defined as

$$\alpha^2 F(\omega) = \frac{1}{N_{E_F}} \sum_{n\mathbf{k},m\mathbf{q},\nu} |g^{\nu}_{n\mathbf{k},m\mathbf{k}+\mathbf{q}}|^2 \delta(\epsilon_{n\mathbf{k}} - E_F) \times \delta(\epsilon_{m\mathbf{k}+\mathbf{q}} - E_F) \delta(\omega - \omega_{\mathbf{q}\nu}), \tag{2}$$

where N_{E_F} is the electronic density of states (DOS) at the Fermi energy (E_F), n and m are band indices, $\mathbf{k}$ is a crystal momentum, $\epsilon_{n\mathbf{k}}$ is a band energy, $\omega_{\mathbf{q}\nu}$ is the phonon frequency of mode ν at wavevector $\mathbf{q}$, and $g^{\nu}_{n\mathbf{k},m\mathbf{k}+\mathbf{q}}$ is the electron-phonon matrix element between a state $n\mathbf{k}$ and $m\mathbf{k}+\mathbf{q}$. We calculated $\alpha^2 F(\omega)$ combining

the SSCHA phonon frequencies and polarization vectors obtained from the Hessian of $E(\boldsymbol{\mathcal{R}})$ with the electron-phonon matrix elements calculated with DFPT. For the Fm-3m and R-3m phases, the electron-phonon matrix elements were calculated in a 6×6×6 **q** point grid and a 40×40×40 **k** point grid. These were combined with the SSCHA phonons and polarization vectors obtained by Fourier interpolation to the 6×6×6 **q** point grid from the real space force constants coming from the Hessian of $E(\boldsymbol{\mathcal{R}})$ in a 3×3×3 supercell for the Fm-3m and in a 2×2×2 supercell for the R-3m. The Dirac deltas on the band energies are estimated by substituting them with a Gaussian of 0.004 Ry width. The calculated $\alpha^2F(\omega)$ functions for the Fm-3m phase are shown in Extended Figures 4 and 5, while in Extended Figure 6 we show the results for the R-3m phase.

Crystal phase diagram exploration. To sample the enthalpy landscape of LaH_{10} we employed the minima hopping method (MHM) [24, 25], which has been successfully used for global geometry optimization in a large variety of applications including superconducting materials such as H_3S, PH_3, and disilane at high pressure [35, 36]. This composition was thoroughly explored with 1, 2, 3 and 4 formula units simulation cells. Variable composition simulations were also performed for other La-H compositions. Energy, atomic forces and stresses were evaluated at the DFT level with the GGA-PBE parametrization to the exchange-correlation functional. A plane wave basis-set with a high cutoff energy of 900 eV was used to expand the wave-function together with the projector augmented wave (PAW) method as implemented in the Vienna Ab Initio Simulation Package VASP [37]. Geometry relaxations were performed with tight convergence criteria such that the forces on the atoms were less than 2 meV/Å and the stresses were less than 0.1 eV/Å^3. Extended Data Figure 1 shows our calculated convex hull of enthalpy formation without considering the zero-point energy at 100, 150 and 200 GPa. Interestingly, there are many stable compositions in the convex hull. LaH_{10} becomes enthalpically stable at ∼125 GPa and remains in the convex well above 300 GPa. Below 150 GPa, R-3m and $C2$ phases (LaH_{10}) show unstable harmonic phonon at Γ, becoming saddle points of $V(\mathbf{R})$. However, harmonically one can find $P1$ stable structures (decreasing symmetry) by following the instability pattern (softening direction, i.e. along eigenvector polarization). $P1$ structures are degenerate in enthalpy within less 3 meV/LaH_{10} with respect $C2$. Hence, we used the $C2$ as a representative of highly distorted structures for our study.

Superconductivity calculations in the Fm-3m phase. Superconductivity calculations were performed within two different approaches that represent the state-of-the-art of *ab initio* superconductivity: Density functional theory for Superconductors (SCDFT) and the Éliashberg equations with full Coulomb interaction.

SCDFT is an extension to DFT for a superconducting ground state [38, 39]. By assuming that the $n\mathbf{k}$ anisotropy in the electron-phonon coupling is negligible (see Ref. 39 for further details), the critical temperature is computed by solving an (isotropic) equation for the Kohn-Sham gap:

$$\Delta_s(\epsilon) = \mathcal{Z}(\epsilon)\Delta_s(\epsilon) - \int d\epsilon' \mathcal{K}(\epsilon,\epsilon') \frac{\tanh\left[\frac{\beta E(\epsilon')}{2}\right]}{2E(\epsilon')} \Delta_s(\epsilon'), \tag{3}$$

where ϵ is the electron energy and β the inverse temperature. The kernels $\mathcal{K}$ and $\mathcal{Z}$ come from the exchange correlation functional of the theory [39–44] and depend on the properties of the pairing interactions: electron-phonon coupling and screened electron-electron repulsion. Eq. 3 allows us to calculate T_c completely *ab initio*, without introducing an empirical μ^* parameter (Coulomb pseudopotential). Dynamic effects on the Coulomb interaction (plasmon) were also tested and did not show any significant effect. In its isotropic form, the screened Coulomb interaction in SCDFT is accounted for by a function $\mu(\epsilon,\epsilon')$, which is given by the average [45] RPA Coulomb matrix element on the iso-energy surfaces ϵ and ϵ' times the DOS at ϵ' ($N(\epsilon')$):

$$\mu(\epsilon,\epsilon') = \sum_{n,m} \iint d^3(kk') V^{RPA}_{n\mathbf{k},m\mathbf{k}'} \frac{\delta(\epsilon-\epsilon_{n\mathbf{k}})}{N(\epsilon_{n\mathbf{k}})} \delta(\epsilon'-\epsilon_{m\mathbf{k}'}). \tag{4}$$

The full energy dependence of the DOS is accounted in the calculations, while the electron-phonon coupling is described by the $\alpha^2F(\omega)$ of Eq. (2).

The second approach we use to simulate the superconducting state is the anisotropic Éliashberg approach [46]. Here we include, together with the energy dependence of the electron DOS, the anisotropy of the electron-phonon coupling. The Green's function form of the Éliashberg equation [46] we solve is given as

$$\Sigma_{n\mathbf{k}}(i\omega_i) = -\frac{1}{N\beta} \sum_{\mu,\mathbf{q},m} V^{\mathrm{ph}}_{mn}(\mathbf{q},i\omega_\mu) G_{m\mathbf{k}+\mathbf{q}}(i\omega_\mu + i\omega_i), \tag{5}$$

$$\Delta_{n\mathbf{k}}(i\omega_i) = -\frac{1}{N\beta} \sum_{\mu,\mathbf{q},m} \{V^{\mathrm{ph}}_{mn}(\mathbf{q},i\omega_\mu) + V^{\mathrm{C}}_{mn}(\mathbf{q},i\omega_\mu)\} \times |G_{m\mathbf{k}+\mathbf{q}}(i\omega_\mu + i\omega_i)|^2 \Delta_{m\mathbf{k}+\mathbf{q}}(i\omega_\mu + i\omega_i). \tag{6}$$

Here, $\Sigma_{n\mathbf{k}}(i\omega_i)$ and $\Delta_{n\mathbf{k}}(i\omega_i)$ are the normal and anomalous self energy, and $V^{\mathrm{ph}}_{mn}(\mathbf{q},i\omega_\mu)$ and $V^{\mathrm{C}}_{mn}(\mathbf{q},i\omega_\mu)$ are the **k**-averaged phonon-mediated interaction and Coulomb interaction, respectively. The explicit form of $V^{\mathrm{ph}}_{mn}(\mathbf{q},i\omega_\mu)$ is given as

$$V^{\mathrm{ph}}_{mn}(\mathbf{q},i\omega_\mu) = \sum_\nu |g^\nu_{nm}(\mathbf{q})|^2 D_\nu(\mathbf{q},i\omega_\mu), \tag{7}$$

where $|g^{\nu}_{nm}(\mathbf{q})|^2$ is a $\mathbf{k}$-averaged electron-phonon matrix element,

$$|g^{\nu}_{nm}(\mathbf{q})|^2 = \frac{\sum_{\mathbf{k}} |g^{\nu}_{n\mathbf{k},m\mathbf{k}+\mathbf{q}}|^2 \delta(\epsilon_{n\mathbf{k}} - E_F)\delta(\epsilon_{m\mathbf{k}+\mathbf{q}} - E_F)}{\sum_{\mathbf{k}} \delta(\epsilon_{n\mathbf{k}} - E_F)\delta(\epsilon_{m\mathbf{k}+\mathbf{q}} - E_F)}, \tag{8}$$

and $D_{\nu}(\mathbf{q}, i\omega_{\mu})$ is a free-phonon Green's function, $D_{\nu}(\mathbf{q}, i\omega_{\mu}) = -2\omega_{\mathbf{q}\nu}/(\omega_{\mu}^2 + \omega_{\mathbf{q}\nu}^2)$. The electron-phonon matrix elements are calculated through a DFPT calculation with 6×6×6 $\mathbf{q}$ point grid, and are combined with the phonon frequencies and polarization vectors obtained by directly Fourier interpolating to this grid the force constants coming from the $E(\boldsymbol{\mathcal{R}})$ Hessian in the 3×3×3 supercell. For the Coulomb interaction, $V^{\mathrm{C}}_{mn}(\mathbf{q}, i\omega_{\mu})$ is approximated by $\mathbf{k}$-averaged static Coulomb interaction within the random phase approximation, $\frac{1}{N_k}\sum_{\mathbf{k}} V^{\mathrm{RPA}}_{m\mathbf{k},n\mathbf{k}+\mathbf{q}}(i\omega_{\mu} = 0)$. Using Eq. (5), the Dyson equation was solved self-consistently and then Eq. (6) was solved to estimate T_c with 36× 36 × 36 $\mathbf{k}$ point grid and 512 Matsubara frequencies.

In Extended Data Table I we summarize all calculated $\mathrm{T_c}$'s within anisotropic ME and isotropic SCDFT. We also include the values obtained with McMillan equation and Allen-Dynes modified McMillan equation (μ^*=0.1). The calculated electron-phonon coupling constant, $\lambda = 2\int_0^{\infty} d\omega \alpha^2 F(\omega)/\omega$, and the logarithmic frequency average, $\omega_{log} = \exp\left(\frac{2}{\lambda}\int_0^{\infty} d\omega \frac{\alpha^2 F(\omega)}{\omega} \log\omega\right)$, are also included in the table.

Quantum structural relaxations in the R-3m and C2 phases. In Extended Figure 7 we show the evolution of the pressure calculated along the different Cartesian directions for the R-3m throughout the SSCHA minimization but keeping the rhombohedral angle fixed at 62.3°. Thus, the centroid positions $\boldsymbol{\mathcal{R}}$ are optimized only considering the internal degrees of freedom of the R-3m phase. Even if at the classical level the stress is isotropic (within a 0.5%), after the SSCHA quantum relaxation an anisotropic stress of a 6% is created between the z and $x-y$ directions. The phonons obtained at the end of the minimization are shown in Extended Figure 6. Secondly, in Extended Figure 8, we show that starting from the result of this minimization but now relaxing also the lattice, the R-3m phase evolves into the Fm-3m phase. It is clear how the pressure calculated with quantum effects becomes isotropic when the rhombohedral angle becomes 60°, the angle corresponding to a fcc lattice in a rhombohedral description. Also it is evident that the Wyckoff positions of the R-3m phase evolve clearly into the Fm-3m Wyckoff positions, which are summarized in Extended Data Table II.

In Extended Data Figure 9 we show the evolution of the diagonal components of the pressure along the three different Cartesian directions for the monoclininc C2 when the lattice structure is relaxed with the SSCHA. The starting point is obtained by first performing a SSCHA relaxation of only internal atomic coordinates keeping the lattice parameters that yield an isotropic stress of 150 GPa. It is clear that quantum effects create an anisotropic stress if the lattice parameters are not modified. When the quantum relaxation of the lattice is performed, the lattice parameters are modified and an isotropic stress is recovered.

Extended Data Figure 10 shows the structures of the R-3m and C2 phases obtained classically and after the quantum SSCHA relaxation. After the quantum relaxation, the symmetry of both structures is recognized as Fm-3m with a tolerance of 0.001 Å for lattice vectors and 0.005 Å for ionic positions, consistent with the stochastic accuracy of the SSCHA. In the same Figure 10, the electronic density of states (DOS) as a function of pressure is plotted. Highly symmetric motif (Fm-3m) maximizes N_{E_F}, while in distorted structures (R-3m and C2) the occupation at the Fermi level is reduced by more than 20 %. This underlines that the classical distortions would lower N_{E_F}, reducing λ, as expected in a system destabilized by the electron-phonon interaction.

Transition temperatures from other La-H compositions. Different compositions on the La-H phase diagram have been reported as thermodynamically stable. Presumably, the stabilization of these compositions and the measurement of different $\mathrm{T_c}$'s (see Drozdov et al. [3]) demonstrate that other stoichiometries are responsible for these measured $\mathrm{T_c}$'s. Notably, these $\mathrm{T_c}$'s appear substantially lower, for instance the values decrease from 250 K, to 215 K, 110 K and to 70 K. Experimentally there is not a clear correlation between sample preparation, $\mathrm{T_c}$ and pressure. In sample preparation of Drozdov et al. pressures can vary from 100 to 200 GPa (gradient inside the diamond anvil cell) and it was proposed that other stoichiometries (low-hydrogen content) are responsible for systematically lower $\mathrm{T_c}$'s.

Conversely, in a later publication the same authors suggested other hydrogen rich system that is enthalpically competitive ($\mathrm{LaH_{11}}$) and possibly responsible for other high-$\mathrm{T_c}$ phases. In order to explore this possibility, we did consider structure prediction runs with this stoichiometry and found crystalline structures that were previously reported in Ref. [47]. Extended Data Figure 11 shows the structural motif and the corresponding phonons and $\alpha^2F(\omega)$ spectral function. We can rule out the possibility that high-$\mathrm{T_c}$, as measured in different samples, arises from $\mathrm{LaH_{11}}$ in its $P4/nmm$ (129) structure (lowest enthalpy structure for this composition at relevant experimental pressures). As seen in Extended Data Figure 11, this phase has a strong molecular crystal character, composed of $\mathrm{H_2}$ units weakly interacting with La-lattice. This phase is indeed a poor metal with low occupation of electrons at the Fermi level due to its molecular character and cannot explain 70 K, or higher values of $\mathrm{T_c}$. Our estimated $\mathrm{T_c}$ with Allen-Dynes formula, harmonic phonons and using a μ^*=0.1 is 7 K at 100 GPa.

[30] John P. Perdew, Kieron Burke, and Matthias Ernzerhof. Generalized gradient approximation made simple. *Phys. Rev. Lett.*, 77:3865, 1996.

[31] Stefano Baroni, Stefano de Gironcoli, Andrea Dal Corso, and Paolo Giannozzi. Phonons and related crystal properties from density-functional perturbation theory. *Rev. Mod. Phys.*, 73:515, 2001.

[32] Paolo Giannozzi, Stefano Baroni, Nicola Bonini, Matteo Calandra, Roberto Car, Carlo Cavazzoni, Davide Ceresoli, Guido L Chiarotti, Matteo Cococcioni, Ismaila Dabo, Andrea Dal Corso, Stefano de Gironcoli, Stefano Fabris, Guido Fratesi, Ralph Gebauer, Uwe Gerstmann, Christos Gougoussis, Anton Kokalj, Michele Lazzeri, Layla Martin-Samos, Nicola Marzari, Francesco Mauri, Riccardo Mazzarello, Stefano Paolini, Alfredo Pasquarello, Lorenzo Paulatto, Carlo Sbraccia, Sandro Scandolo, Gabriele Sclauzero, Ari P Seitsonen, Alexander Smogunov, Paolo Umari, and Renata M Wentzcovitch. Quantum espresso: a modular and open-source software project for quantum simulations of materials. *Journal of Physics: Condensed Matter*, 21:395502, 2009.

[33] P Giannozzi, Oliviero Andreussi, T Brumme, O Bunau, M Buongiorno Nardelli, M Calandra, R Car, C Cavazzoni, D Ceresoli, M Cococcioni, et al. Advanced capabilities for materials modelling with quantum espresso. *Journal of Physics: Condensed Matter*, 29:465901, 2017.

[34] Ion Errea, Matteo Calandra, and Francesco Mauri. First-principles theory of anharmonicity and the inverse isotope effect in superconducting palladium-hydride compounds. *Phys. Rev. Lett.*, 111:177002, 2013.

[35] A. José Flores-Livas, Antonio Sanna, and E.K.U. Gross. High temperature superconductivity in sulfur and selenium hydrides at high pressure. *Eur. Phys. J. B*, 89:1, 2016.

[36] José A. Flores-Livas, Maximilian Amsler, Christoph Heil, Antonio Sanna, Lilia Boeri, Gianni Profeta, Chris Wolverton, Stefan Goedecker, and E. K. U. Gross. Superconductivity in metastable phases of phosphorus-hydride compounds under high pressure. *Phys. Rev. B*, 93:020508, 2016.

[37] G. Kresse and J. Furthmüller. Efficiency of ab-initio total energy calculations for metals and semiconductors using a plane-wave basis set. *Comput. Mat. Sci.*, 6:15, 1996.

[38] L. N. Oliveira, E. K. U. Gross, and W. Kohn. Density-functional theory for superconductors. *Phys. Rev. Lett.*, 60:2430, 1988.

[39] M. Lüders, M. A. L. Marques, N. N. Lathiotakis, A. Floris, G. Profeta, L. Fast, A. Continenza, S. Massidda, and E. K. U. Gross. Ab-initio theory of superconductivity. i. density functional formalism and approximate functionals. *Phys. Rev. B*, 72:024545, 2005.

[40] José A. Flores-Livas and Antonio Sanna. Superconductivity in intercalated group-iv honeycomb structures. *Phys. Rev. B*, 91:054508, 2015.

[41] Camilla Pellegrini, Henning Glawe, Antonio Sanna. Density functional theory of superconductivity in doped tungsten oxides. *Phys. Rev. Materials*, 3:064804, 2019.

[42] M. A. L. Marques, M. Lüders, N. N. Lathiotakis, G. Profeta, A. Floris, L. Fast, A. Continenza, E. K. U. Gross, and S. Massida. Ab initio theory of superconductivity. II. Application to elemental metals. *Phys. Rev. B*, 72:024546, 2005.

[43] A. Linscheid, A. Sanna, A. Floris, and E. K. U. Gross. First-principles calculation of the real-space order parameter and condensation energy density in phonon-mediated superconductors. *Phys. Rev. Lett.*, 115:097002, 2015.

[44] S. Massidda, F. Bernardini, C. Bersier, A. Continenza, P. Cudazzo, A. Floris, H. Glawe, M. Monni, S. Pittalis, G. Profeta, A. Sanna, S. Sharma, and E. K. U. Gross. The role of coulomb interaction in the superconducting properties of CaC6 and H under pressure. *Superconductor Science and Technology*, 22:034006, 2009.

[45] Antonio Sanna, José A. Flores-Livas, Arkadiy Davydov, Gianni Profeta, Kay Dewhurst, Sangeeta Sharma, and E. K. U. Gross. Ab initio Eliashberg Theory: Making Genuine Predictions of Superconducting Features. *J. Phys. Soc. Jpn.*, 87:041012, 2018.

[46] W. Sano, T. Koretsune, T. Tadano, R. Akashi, and R. Arita. Effect of Van Hove singularities on high-T_c superconductivity in H_3S. *Phys. Rev. B*, 93:094525, 2016.

[47] Feng Peng, Ying Sun, Chris J. Pickard, Richard J. Needs, Qiang Wu, and Yanming Ma. Hydrogen clathrate structures in rare earth hydrides at high pressures: Possible route to room-temperature superconductivity. *Phys. Rev. Lett.*, 119:107001, 2017.

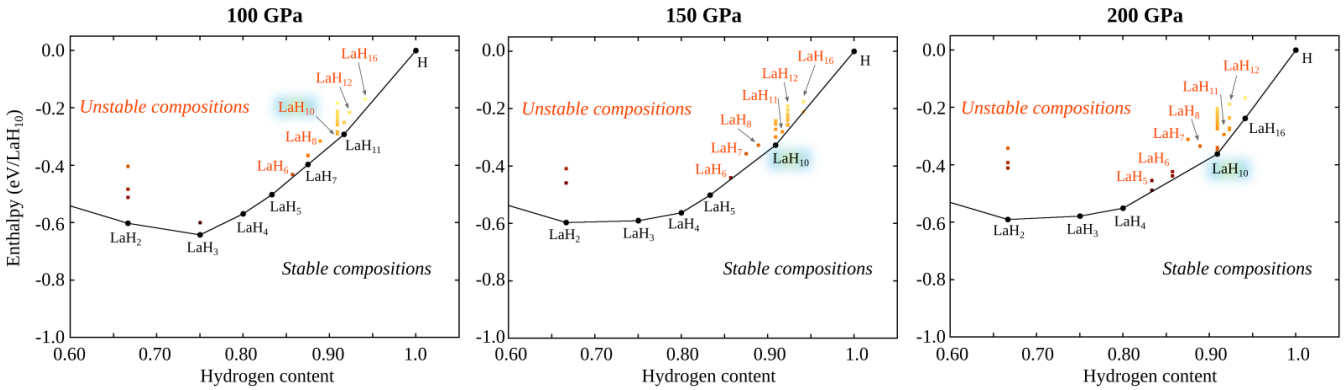

Extended Data Figure 1. **Convex hull of enthalpy formation.** It is noticeable that at low pressure (left panel, 100 GPa) the composition of LaH_{10} is not stable and only develops as stable point in the convex hull above ∼125 GPa.

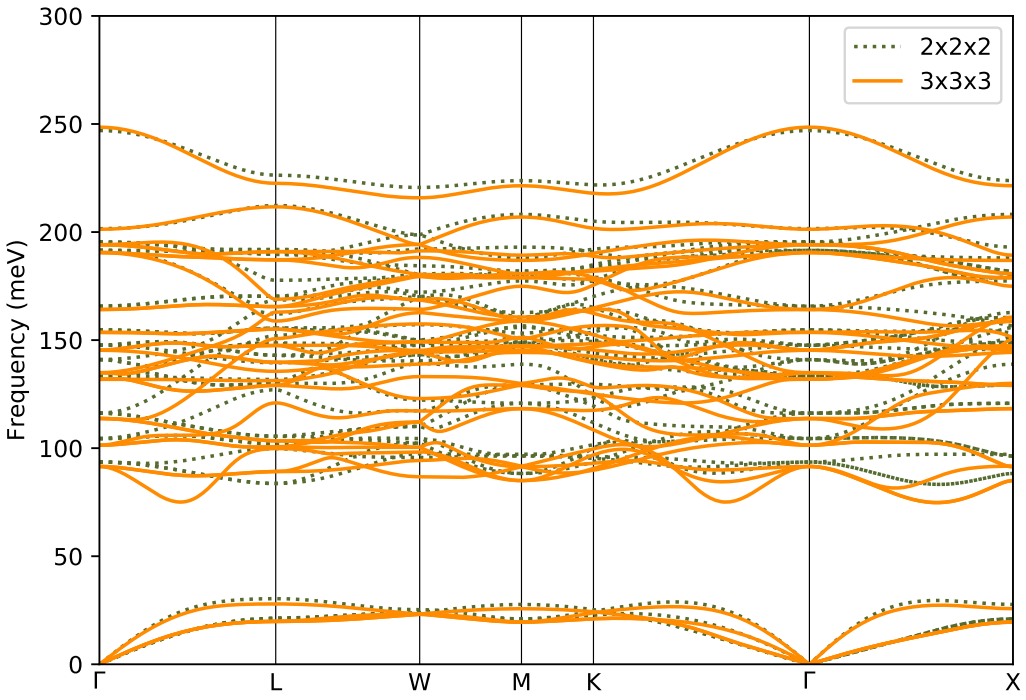

Extended Data Figure 2. **SSCHA phonons supercell convergence for LaH_{10} at 163 GPa.** The phonon spectra shown are calculated by directly Fourier interpolating the force constants obtained from the Hessian of $E(\boldsymbol{\mathcal{R}})$ in a real space $2 \times 2 \times 2$ and a $3 \times 3 \times 3$ supercell. The similarity of both phonon spectrum obtained by Fourier interpolation indicates that these SSCHA force constants are short-ranged and can be Fourier interpolated.

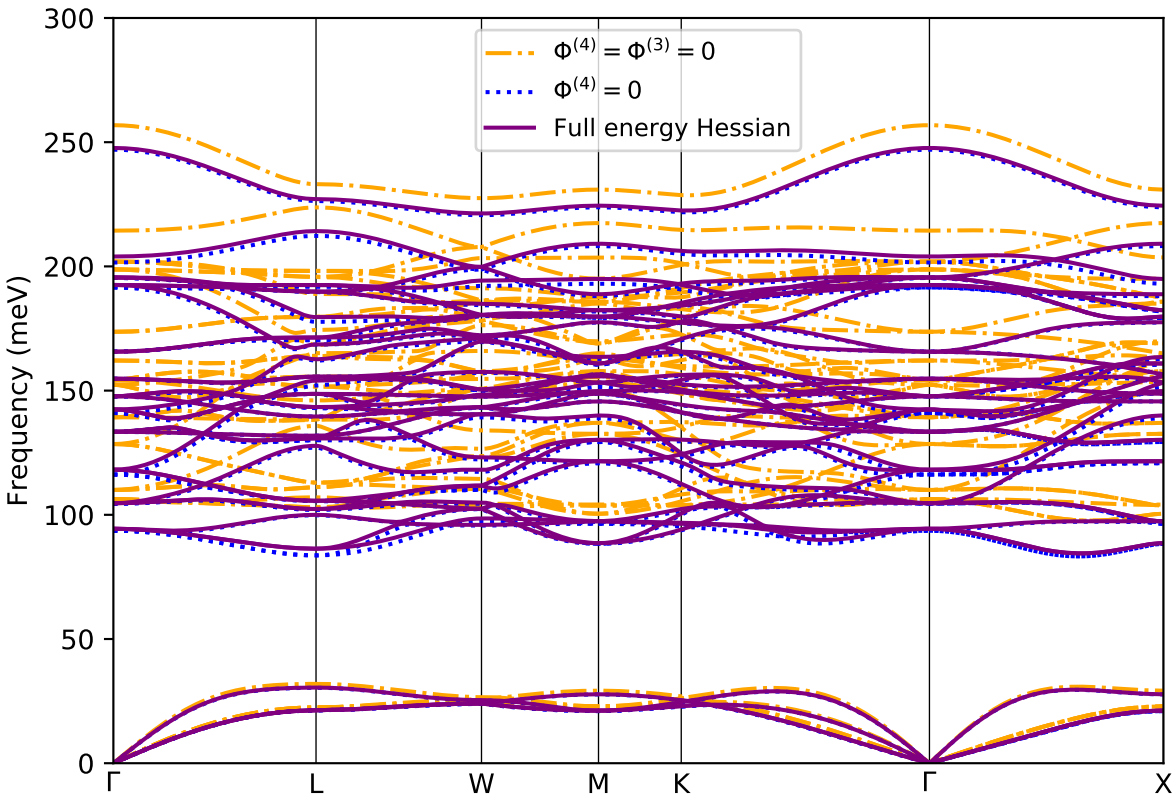

Extended Data Figure 3. **Different anharmonic phonons calculated for LaH_{10} at 163 GPa.** Phonon spectra obtained from the SSCHA energy Hessian of Eq. (1) making different level of approximations. The purple solid line is the phonon spectrum calculated with the full energy Hessian, without any approximation. In the blue dotted spectrum we set $\overset{(4)}{\mathbf{\Phi}} = 0$ in the equation. In the orange dash-dotted line we set $\overset{(3)}{\mathbf{\Phi}} = \overset{(4)}{\mathbf{\Phi}} = 0$, so that the phonon spectra corresponds to the one coming directly from the SSCHA variational force constants $\mathbf{\Phi}$. The results clearly show that while the effect of $\overset{(3)}{\mathbf{\Phi}}$ is important, setting $\overset{(4)}{\mathbf{\Phi}} = 0$ is perfectly safe. All these phonon spectra in the figures are obtained by Fourier interpolating directly the real space anharmonic force constants in a $2 \times 2 \times 2$ supercell.

Extended Data Table I. **Summary of calculated superconducting T_c.** Values are within different approaches ranging from empirical to fully *ab initio*: McMillan equation ($T_{c\mu^*=0.1}^{Mc}$), Allen-Dynes modified McMillan equation ($T_{c\mu^*=0.1}^{AD}$), anisotropic treatment of Migdal-Éliashberg ($T_{c ani}^{ME}$) and SCDFT (T_c^{SCDFT}). Values of λ and ω_{log} are also given.

System	Pressure (GPa)	λ	ω_{log} (meV)	$T_{c\mu^*=0.1}^{Mc}$ (K)	$T_{c\mu^*=0.1}^{AD}$ (K)	$T_{c ani}^{ME}$ (K)	T_c^{SCDFT} (K)
LaH_{10}	129	3.62	76.4	171.8	252.6	255.3	230
LaH_{10}	163	2.67	96.4	197.1	247.0	242.8	225
LaH_{10}	214	2.06	115.5	196.3	235.9	237.9	210
LaH_{10}	264	1.73	126.6	189.5	219.2	216.9	201
LaD_{10}	159	3.14	63.5	135.0	184.2	180.4	171
LaD_{10}	210	2.21	81.7	145.5	176.5	172.9	158
LaD_{10}	260	1.80	92.2	142.2	164.6	157.9	151

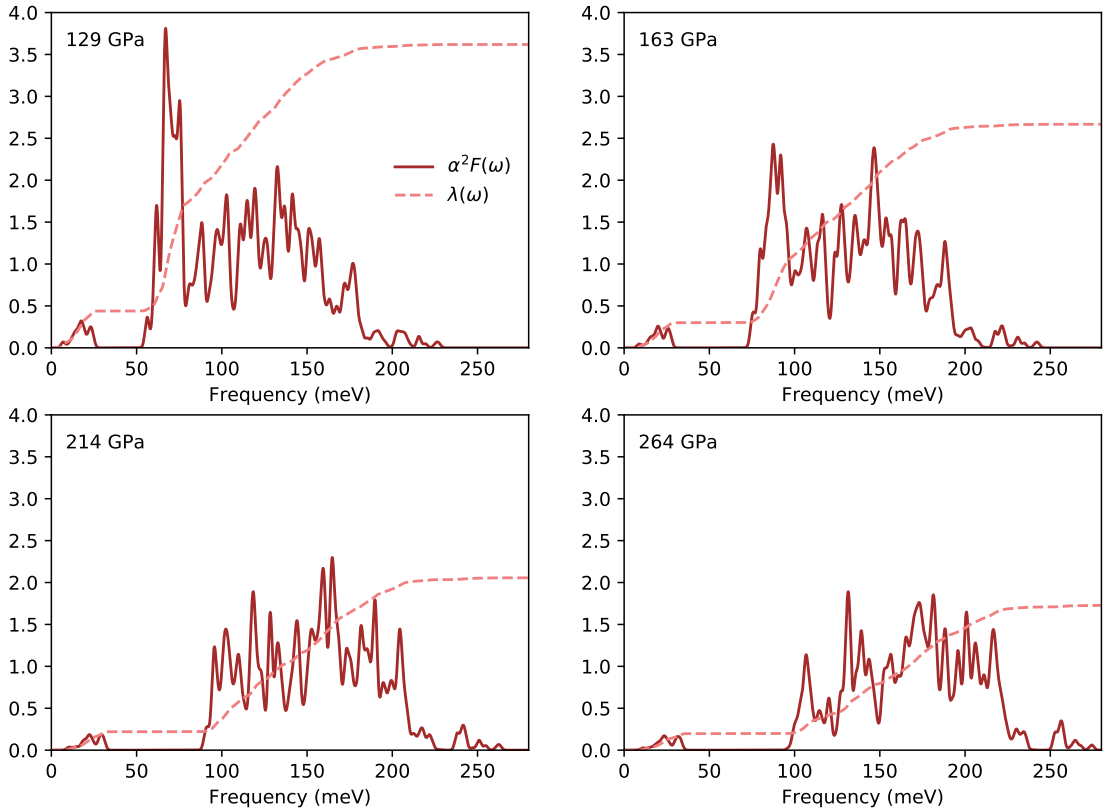

Extended Data Figure 4. $\alpha^2F(\omega)$ **for the** Fm-$3m$ **phase of LaH**$_{10}$**.** Calculated $\alpha^2F(\omega)$ for different pressures together with the integrated electron-phonon coupling constant, which is defined as $\lambda(\omega) = 2\int_0^\omega d\Omega\alpha^2F(\Omega)/\Omega$. The results show that optical modes, who have hydrogen character, are responsible for the large value of the electron-phonon coupling constant λ. It is worth noting, however, that acoustic modes with La character contribute between 0.2 and 0.5 to λ and cannot be neglected to estimate T_c correctly.

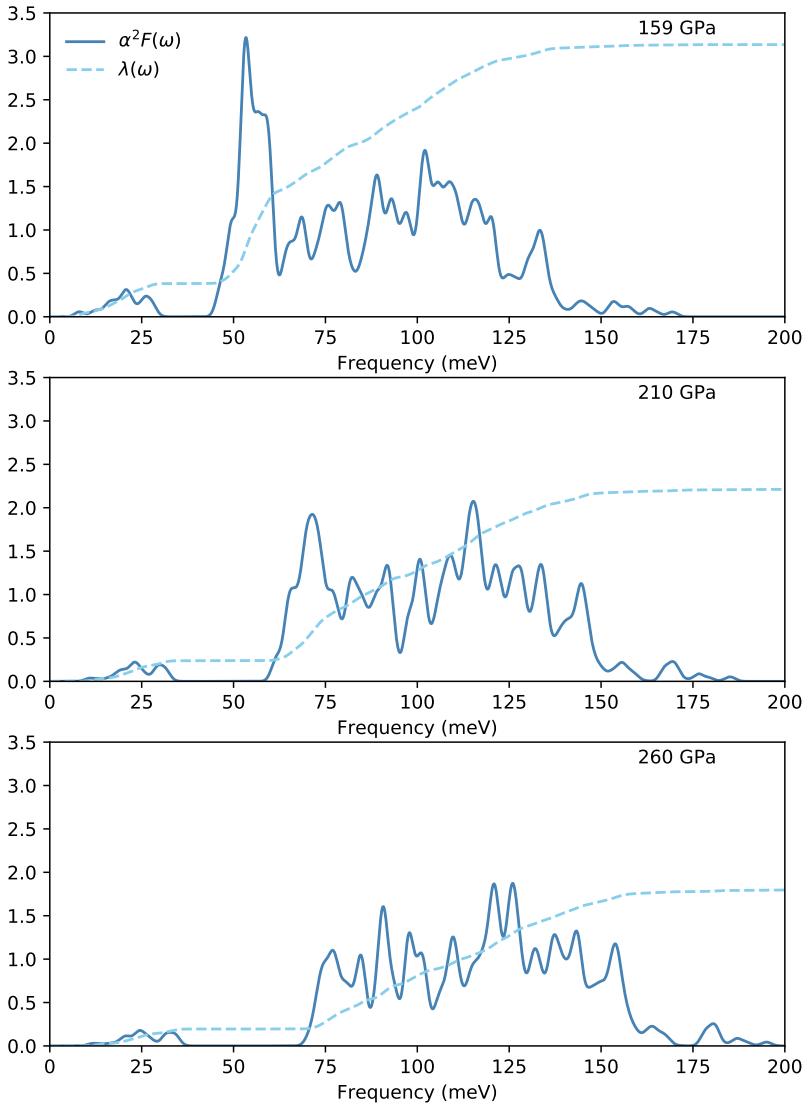

Extended Data Figure 5. $\alpha^2F(\omega)$ **for the** Fm-$3m$ **phase of LaD**$_{10}$**.** The integrated electron-phonon coupling constant $\lambda(\omega)$ is also shown.

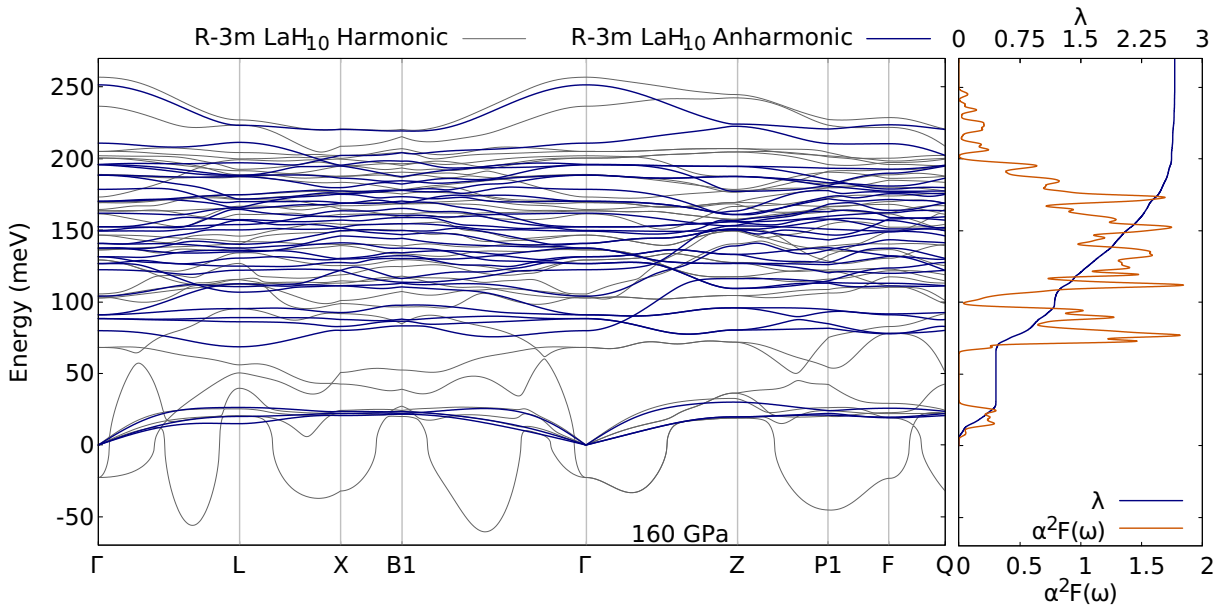

Extended Data Figure 6. **Phonon dispersion of LaH_{10} on the rhombohedral phase.** Harmonic and anharmonic phonon spectrum keeping a 62.3° rhombohedral angle. The harmonic calculation is performed with the internal atomic positions that yield classical vanishing forces. The anharmonic calculation is performed after relaxing with the SSCHA the internal degrees of freedom but keeping the 62.3° rhombohedral angle. At the harmonic level there are unstable phonon modes even at Γ. Symmetry prevents the relaxation of this structure according to the unstable phonon mode at Γ. The harmonic phonons are calculated at a classic pressure of 150 GPa. Quantum effects add an extra ∼10 GPa to the pressure. On the right side of the figure is also shown the behavior of $\lambda(\omega)$ and $\alpha^2F(\omega)$ for the anharmonic calculation.

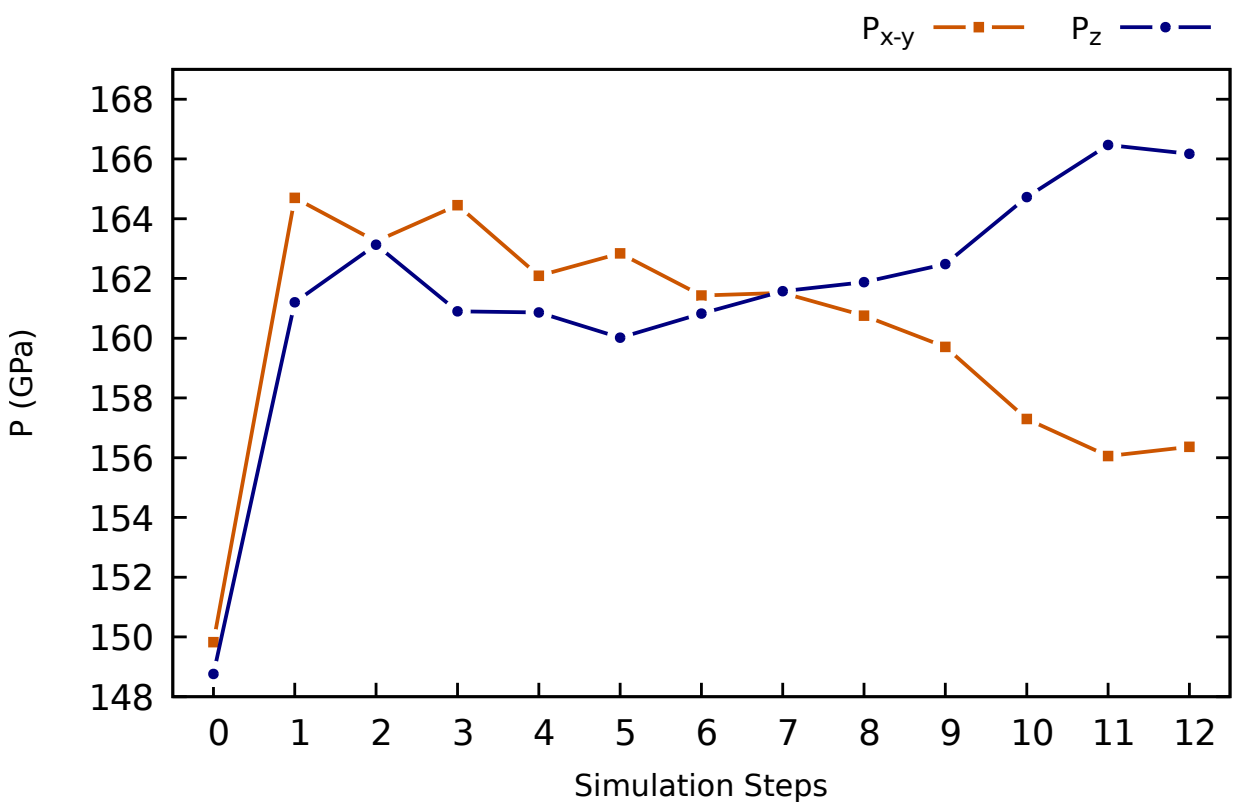

Extended Data Figure 7. **Anisotropic pressure of the R-3m phase of LaH_{10} in a fixed-cell quantum relaxation.** Pressure along the different Cartesian directions during the SSCHA relaxation of the internal parameters keeping the rhombohedral angle at 62.3° fixed. At step 0 the pressure reported is obtained directly from $V(\mathbf{R})$, neglecting quantum effects. It is isotropic within one GPa of difference between the $x-y$ and z directions. At the other steps it is calculated from the quantum $E(\boldsymbol{\mathcal{R}})$ and along the minimization it becomes anisotropic. When the minimization stops at step 12, i.e., the internal coordinates are at the minimum of the $E(\boldsymbol{\mathcal{R}})$ for this lattice, the stress anisotropy between z and $x-y$ directions is about 6%. This clearly indicates that quantum effects want to relax the crystal lattice, in particular, since P_z is larger, by reducing the rhombohedral angle. It is worth noting that quantum effects approximately increase the total pressure by 10 GPa, which is calculated as $P = (P_x + P_y + P_z)/3$. The initial cell parameters before the minimization are $a = 3.5473398$ Å and $\alpha = 62.34158$ ° . The initial values of the free Wyckoff parameters, which yield classical vanishing forces and a 150 GPa isotropic stress, are $\epsilon_a = 0.26043$, $\epsilon_b = 0.09950$, $\epsilon_x = 0.10746$ and $\epsilon_y = 0.12810$. Check the Extended Data Table II for more details.

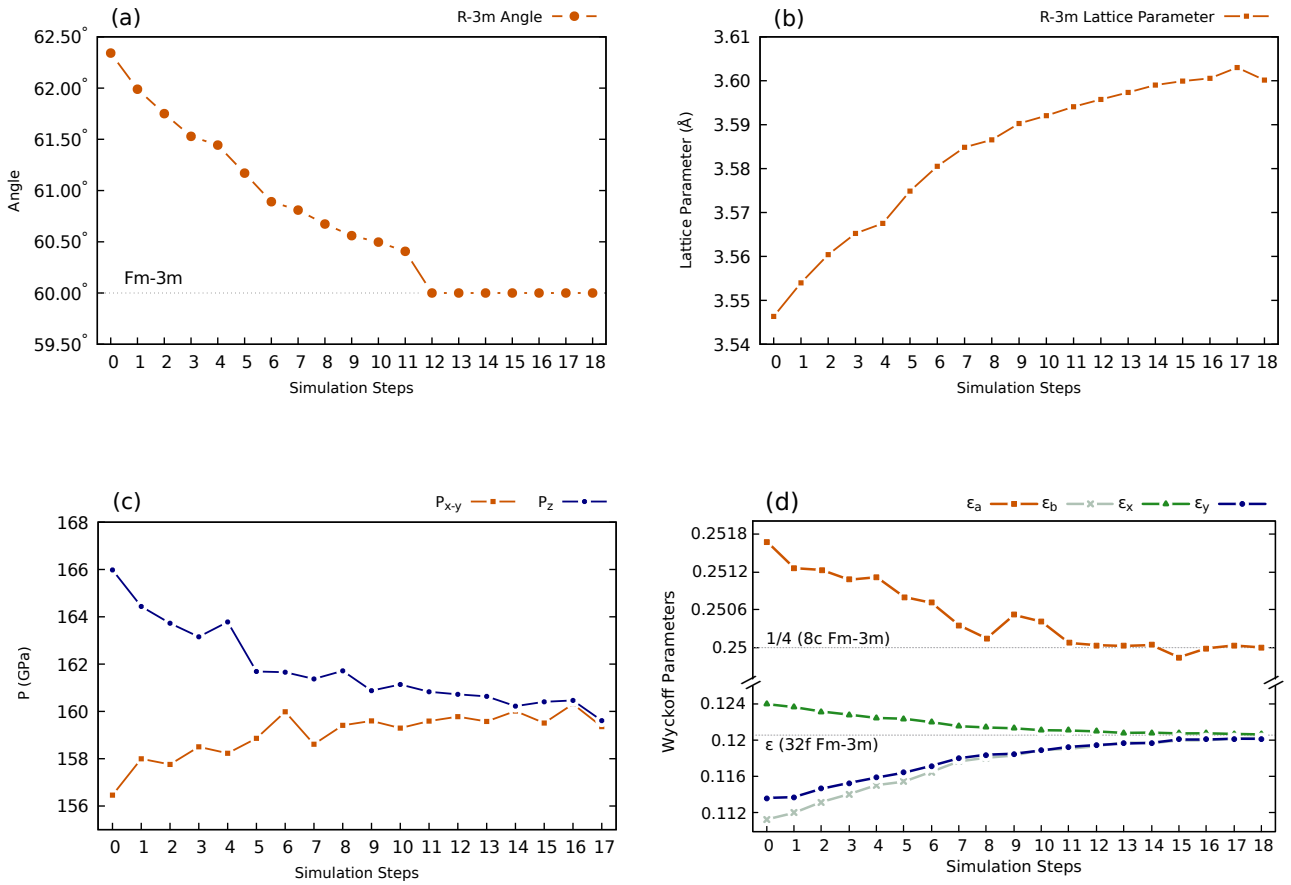

Extended Data Figure 8. **Details on the R-3m LaH_{10} cell relaxation including quantum effects.** The initial point for the relaxation is the output from the previous internal relaxation with fixed angle presented in Extended Figure 7. The R-3m phase in the rhombohedral description is described by three vectors of the same length ($a = b = c$) and by the angle between them ($\alpha = \beta = \gamma$). In panel **(a)** we show the evolution of the rhombohedral angle and in panel **(b)** the evolution of the rhombohedral lattice parameter ($|\mathbf{a}| = |\mathbf{b}| = |\mathbf{c}|$). The evolution of the stress tensor in the quantum SSCHA minimization is shown in panel **(c)**. It is clear that in the end of the minimization the structure obtains a 60° angle, which matches the angle of a fcc lattice, and that in this case the stress is isotropic. In panel **(d)** we show the evolution of the Wyckoff positions in the minimization and we compare it with those of the Fm-3m. The occupied Wyckoff positions for both R-3m LaH_{10} and Fm-3m LaH_{10} are summarized in the Extended Data Table II. Here, it can be seen the evolution of ϵ_a, ϵ_b, ϵ_x, and ϵ_y parameters in the minimization. The atoms in the first set of 6c positions approach the 8c Wyckoff site of the Fm-3m, while the atoms in the second set of 6c positions and those in 18h sites approach the atoms in the 32f Wyckoff site of the Fm-3m, where $\epsilon = 0.12053$.

Extended Data Table II. R-3m **LaH$_{10}$ and** Fm-3m **LaH$_{10}$ Wycokff positions.** The table summarizes the occupied Wyckoff positions for the two structures. We describe the Wyckoff positions in crystal coordinates so that the $[x, y, z]$ coordinate should be understood as a $x\mathbf{a} + y\mathbf{b} + z\mathbf{c}$ atomic position with **a**, **b**, **c** the lattice vectors. For the R-3m phase we use the rhombohedral lattice (R), where the three lattice vectors have the same length ($a = b = c$) and the angle between them is the same ($\alpha = \beta = \gamma$). The Fm-3m phase is described both in this rhombohedral description (R) and, for comparison, in the standard cubic conventional lattice (C). In the Fm-3m the lanthanum atom is described by the **4b** sites, two hydrogen atoms occupy the **8c** sites, and the remaining 8 hydrogen atoms occupy the **32f** sites. Most of the atomic positions are fixed by symmetry and overall the Fm-3m structure can be described by one single free parameter (ϵ). In the R-3m the lanthanum atom is locked in the **3b** sites, two pairs of hydrogen atoms occupy the **6c** sites, and the remaining 6 hydrogen atoms occupy the **18h** sites. In this case symmetry allows for more freedom, and overall the structure of the R-3m phase can be described by 4 free parameters (ϵ_a, ϵ_b, ϵ_x and ϵ_y).

Fm-3m (C)		Fm-3m (R)		R-3m (R)	
1 La **4b**	$[\frac{1}{2}, \frac{1}{2}, \frac{1}{2}]$	1 La **4b**	$[\frac{1}{2}, \frac{1}{2}, \frac{1}{2}]$	1 La **3b**	$[\frac{1}{2}, \frac{1}{2}, \frac{1}{2}]$
2 H **8c**	$[\frac{1}{4}, \frac{1}{4}, \frac{1}{4}]$	2 H **8c**	$[\frac{1}{4}, \frac{1}{4}, \frac{1}{4}]$	2 H **6c**	$[\epsilon_a, \epsilon_a, \epsilon_a]$
	$[\frac{3}{4}, \frac{3}{4}, \frac{3}{4}]$		$[\frac{3}{4}, \frac{3}{4}, \frac{3}{4}]$		$[-\epsilon_a, -\epsilon_a, -\epsilon_a]$
8 H **32f**	$[\epsilon,\epsilon,\epsilon]$	8 H **32f**	$[\epsilon,\epsilon,\epsilon]$	2 H **6c**	$[\epsilon_b,\epsilon_b,\epsilon_b]$
	$[-\epsilon,-\epsilon,-\epsilon]$		$[-\epsilon,-\epsilon,-\epsilon]$		$[-\epsilon_b,-\epsilon_b,-\epsilon_b]$
	$[\epsilon,\epsilon,-\epsilon]$		$[-\epsilon,-\epsilon,3\epsilon]$	6 H **18h**	$[-\epsilon_x,-\epsilon_x,3\epsilon_y]$
	$[\epsilon,-\epsilon,\epsilon]$		$[-\epsilon,3\epsilon,-\epsilon]$		$[-\epsilon_y,3\epsilon_x,-\epsilon_x]$
	$[-\epsilon,\epsilon,\epsilon]$		$[3\epsilon,-\epsilon,-\epsilon]$		$[3\epsilon_y,-\epsilon_x,-\epsilon_x]$
	$[-\epsilon,-\epsilon,\epsilon]$		$[\epsilon,\epsilon,-3\epsilon]$		$[\epsilon_x,\epsilon_x,-3\epsilon_y]$
	$[-\epsilon,\epsilon,-\epsilon]$		$[\epsilon,-3\epsilon,\epsilon]$		$[\epsilon_x,-3\epsilon_y,\epsilon_x]$
	$[\epsilon,-\epsilon,-\epsilon]$		$[-3\epsilon,\epsilon,\epsilon]$		$[-3\epsilon_y,\epsilon_x,\epsilon_x]$

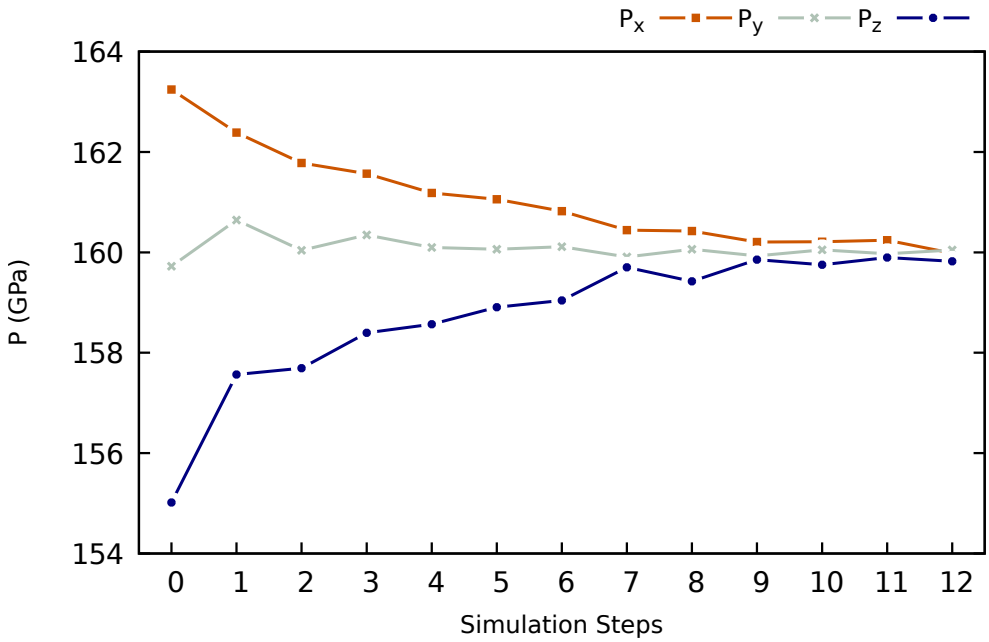

Extended Data Figure 9. **Anisotropic pressure of the $C2$ phase of LaH$_{10}$ in a cell quantum relaxation.** The figure shows the pressures along the different Cartesian directions during the SSCHA cell minimization. The target pressure for this minimization is 160 GPa. At the end of the minimization the isotropy of the stress tensor is recovered. A symmetry analysis performed on the structure at the end of the minimization confirms the $C2$ LaH$_{10}$ evolves in the Fm-3m LaH$_{10}$. The initial values $P_x = 163.2$ (GPa), $P_y = 159.7$(GPa), $P_z = 155.0$(GPa) are obtained by an atomic internal relaxation performed using the SSCHA with fixed cell.

Extended Data Table III. **Crystal structure details for relevant phases**. Lattice parameters and atomic coordinates for LaH_{10} ($Immm$) and LaH_{10} ($C2$) at 150 GPa and LaH_{11} $P4/nmm$ at 100 GPa. These pressures are estimated classically. The positions below give vanishing forces at classical level.

Composition (Space group)	Lattice parameters	Wyckoff positions
LaH_{10} ($Immm$)	$a = 3.58303$ Å	La **2c** [0.50000, 0.50000, 0.00000]
	$b = 3.61834$ Å	H **8m** [0.75841, 0.00000, 0.11649]
	$c = 5.08749$ Å	H **8l** [0.00000, 0.75742, 0.87548]
		H **4j** [0.50000, 0.00000, 0.74572]
LaH_{10} ($C2$)	$a = 6.15468$ Å	La **4c** [0.49244, 0.00070, 0.25292]
	$b = 3.60628$ Å	H **4c** [0.13978, 0.24567, -0.05243]
	$c = 7.23776$ Å	H **4c** [0.09798, 0.24122, 0.45027]
	$\beta = 55.71434°$	H **4c** [0.36015, 0.25590, 0.05238]
		H **4c** [0.40204, 0.26021, 0.54971]
		H **4c** [-0.09751, 0.00051, -0.05100]
		H **4c** [0.86810, 0.00071, 0.43706]
		H **4c** [0.88713, 0.00076, 0.69398]
		H **4c** [0.87083, 0.00068, 0.19089]
		H **4c** [0.73058, 0.00043, 0.88088]
		H **4c** [0.76156, 0.00071, 0.36763]
LaH_{11} ($P4/nmm$)	$a = 3.87435$ Å	La **2c** [0.25000, 0.25000, 0.78577]
	$b = 3.87435$ Å	H **4e** [0.00000, 0.00000, 0.50000]
	$c = 5.27636$ Å	H **8i** [0.25000, -0.02052, 0.17824]
		H **8i** [0.25000, 0.55418, 0.35160]
		H **2a** [0.75000, 0.25000, 0.00000]

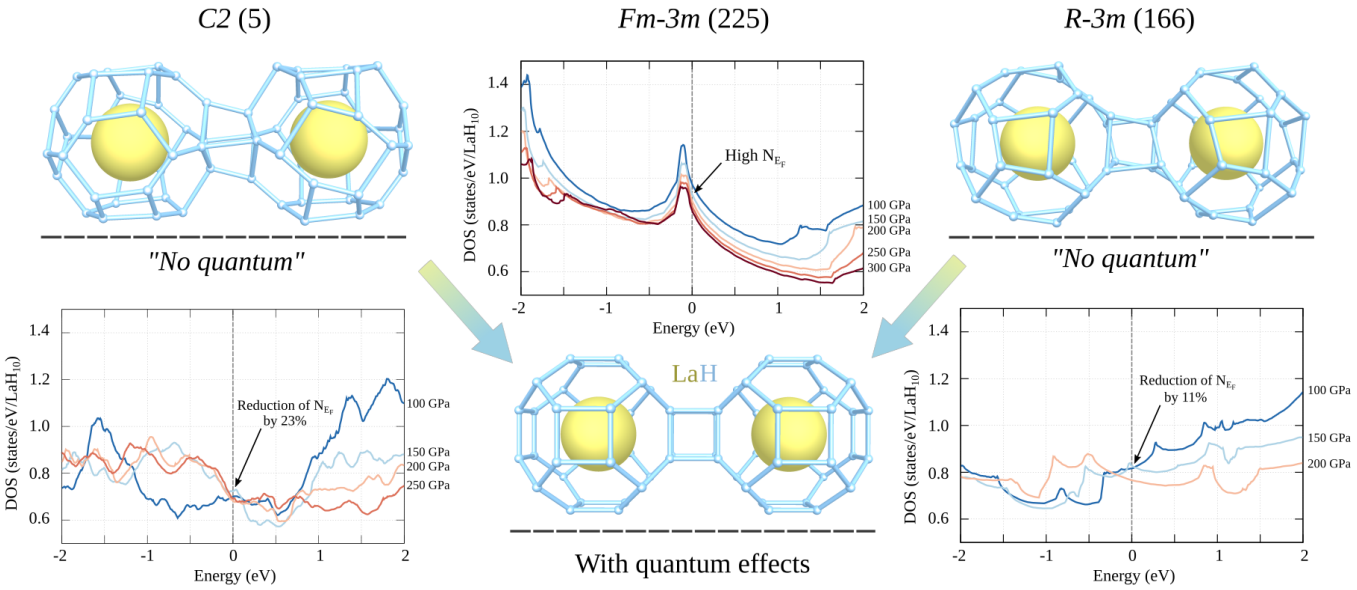

Extended Data Figure 10. **SSCHA minimization on LaH_{10} and DOS.** Top figures: two initial structures ($C2$ and R-$3m$) low enthalpy, considered in our SSCHA simulations. When considering quantum effects both structures evolve towards the Fm-$3m$ structure. Corresponding total electronic density of states (DOS) as a function of pressure are plotted for each structure (for comparison in the same energy scale). Highly symmetric motif (Fm-$3m$) maximizes N_{E_F}, while in distorted structures (R-$3m$ and $C2$) the occupation at the Fermi level is reduced by more than 23 % for $C2$ and by 11 % for R-$3m$, both comparison at 150 GPa w.r.t. Fm-$3m$. Classical pressures are appended for comparison in DOS panels. Note that DOS shape is also strongly modified.

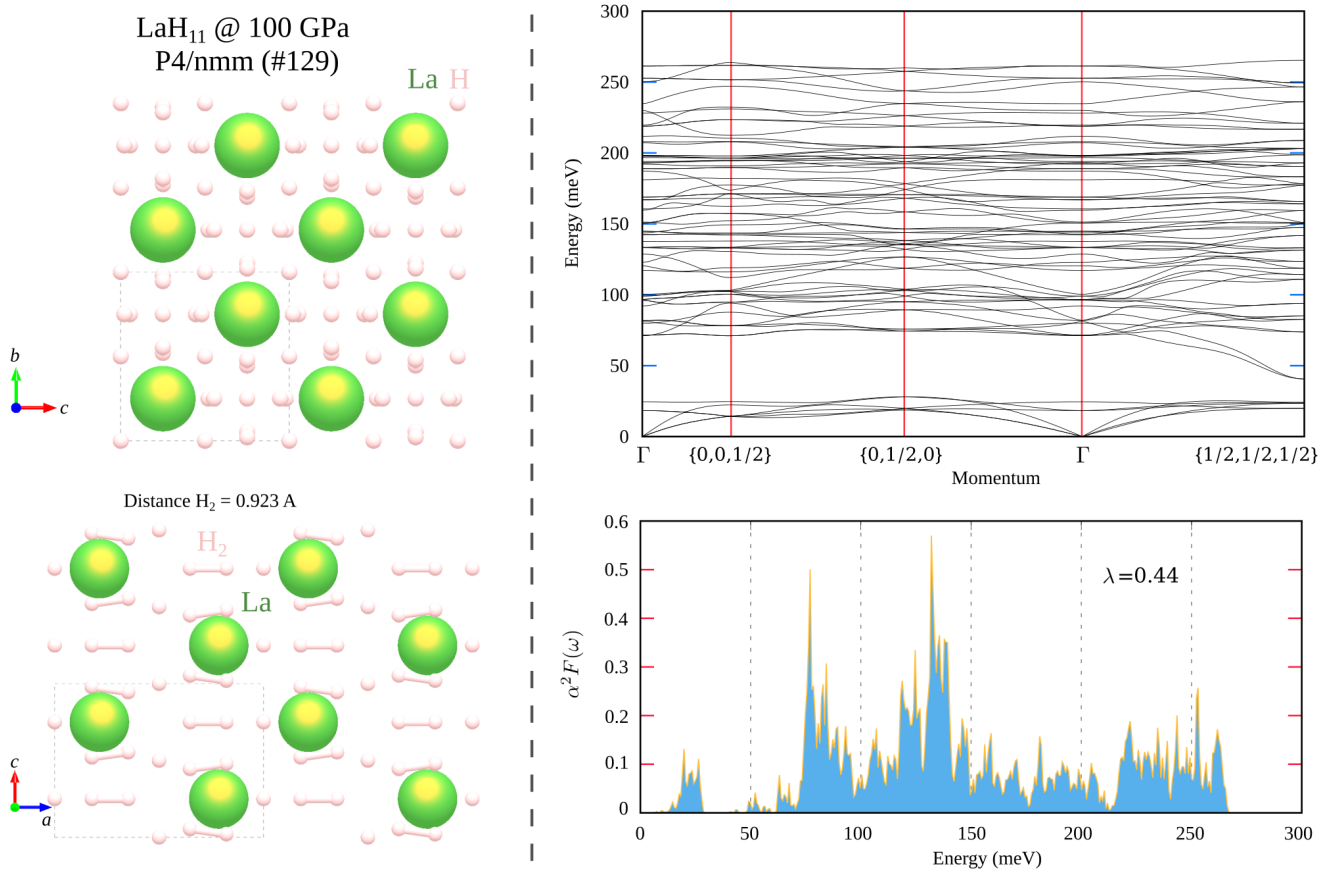

Extended Data Figure 11. **Details on LaH_{11}.** Left: $P4/nmm$ crystal structure of LaH_{11} at 100 GPa thermodynamically stable in the convex hull. Right top: harmonic phonons dispersion along momentum space for this composition: it is dynamically stable. Right bottom: superconducting Éliashberg spectrum function ($\alpha^2F(\omega)$) calculated for this composition at the pressure indicated with harmonic phonons. The estimated T_c with Allen-Dynes formula (μ^*=0.1) is ~7 K at 100 GPa (harmonic phonons).